ACS APPLIED MATERIALS & INTERFACES

Research Article

www.acsami.org

Graphene/Fe_2O_3/SnO_2 Ternary Nanocomposites as a High-Performance Anode for Lithium Ion Batteries

Guofeng Xia,[†,§] Ning Li,*[,†] Deyu Li,[†] Ruiqing Liu,[†] Chen Wang,[†] Qing Li,[‡] Xujie Lü,[‡] Jacob S. Spendelow,[‡] Junliang Zhang,[§] and Gang Wu*[,‡]

[†]School of Chemical Engineering and Technology, Harbin Institute of Technology, Harbin 150001, China

[‡]Materials Physics and Applications Division, Los Alamos National Laboratory, Los Alamos, New Mexico 87545, United States

[§]School of Mechanical Engineering, Shanghai Jiao Tong University, Shanghai 200240, China

Supporting Information

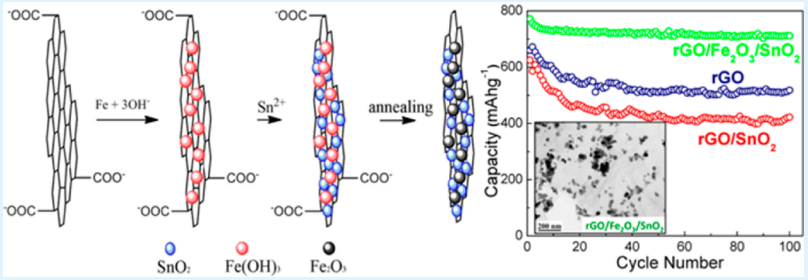

ABSTRACT: We report an rGO/Fe_2O_3/SnO_2 ternary nanocomposite synthesized via homogeneous precipitation of Fe_2O_3 nanoparticles onto graphene oxide (GO) followed by reduction of GO with $SnCl_2$. The reduction mechanism of GO with $SnCl_2$ and the effects of reduction temperature and time were examined. Accompanying the reduction of GO, particles of SnO_2 were deposited on the GO surface. In the graphene nanocomposite, Fe_2O_3 nanoparticles with a size of ~20 nm were uniformly dispersed surrounded by SnO_2 nanoparticles, as demonstrated by transmission electron microscopy analysis. Due to the different lithium insertion/extraction potentials, the major role of SnO_2 nanoparticles is to prevent aggregation of Fe_2O_3 during the cycling. Graphene can serve as a matrix for Li^+ and electron transport and is capable of relieving the stress that would otherwise accumulate in the Fe_2O_3 nanoparticles during Li uptake/release. In turn, the dispersion of nanoparticles on graphene can mitigate the restacking of graphene sheets. As a result, the electrochemical performance of rGO/Fe_2O_3/SnO_2 ternary nanocomposite as an anode in Li ion batteries is significantly improved, showing high initial discharge and charge capacities of 1179 and 746 $mAhg^{-1}$, respectively. Importantly, nearly 100% discharge−charge efficiency is maintained during the subsequent 100 cycles with a specific capacity above 700 $mAhg^{-1}$.

KEYWORDS: *lithium ion batteries, anode materials, Fe_2O_3, SnO_2, reduced graphene oxide, graphene nanocomposites*

INTRODUCTION

Lithium ion batteries (LIBs) with high energy and power densities are highly desirable for electric vehicle (EV) applications. The anodes of LIBs constructed using layered graphite materials are capable of storing ions in the material's bulk but suffer from low energy and power density. The graphite anode can only intercalate one Li atom per six carbon atoms (LiC_6) with a theoretical capacity of 372 $mAhg^{-1}$.[1] Strategies for developing new materials with fast electron transport, large capacity, and efficient lithium ion diffusion will lead to high-power and high-rate LIBs for transportation applications.[2−5] Thus, attention on the anode has been shifting from traditional graphite to other advanced materials with an aim to increase the number of lithiation sites and improve the diffusivity of Li.[6−9]

Among various anode materials for LIBs, transition metal oxides, such as Co_3O_4, CuO, Fe_2O_3, and SnO_2, have attracted substantial attention due to their high theoretical specific capacities. The lithium storage mechanism of these transition metal oxides is based on the reversible formation/decomposition of Li_2O catalyzed by the transition metal nanograins,[8,10] the so-called displacive redox reaction.[11] In particular, Fe_2O_3 has great potential for commercial applications due to its high capacity (1005 $mAhg^{-1}$), low toxicity, and cost effectiveness.[5,12−16] Another promising oxide anode material is SnO_2 with high theoretical capacity and low working potential (~0.6 V vs Li/Li^+).[9,17−20] The lithium storage mechanism of SnO_2 is composed of an irreversible and a reversible step:[17]

$$SnO_2 + 4Li^+ + 4e^- \rightarrow Sn + 2Li_2O \quad (1)$$

Received: June 2, 2013
Accepted: August 15, 2013
Published: August 15, 2013

$$Sn + xLi^+ + xe^- \leftrightarrow Li_xSn \quad (0 \le x \le 4.4) \qquad (2)$$

On the basis of the second reversible alloying reaction, SnO_2 exhibits an attractive theoretical capacity of 780 $mAhg^{-1}$.[21] However, Li-ion insertion/extraction cycling leads to significant volume expansion/shrinkage of Fe_2O_3 or SnO_2 materials, resulting in particle fracture and battery capacity loss.[22,23] Recent studies have suggested that cycling-induced strain could be prevented through introduction of nanosized materials[24−26] or integration of effective structural buffers such as carbon materials,[8,20] thereby improving cycle stability.

Graphene materials, possessing high electron conductivity, large specific surface area (up to 2600 $m^2\ g^{-1}$), and a broad window of electrochemical stability, hold great promise as an advanced material for energy storage technologies.[27−30] The specific capacity of graphene for Li can be substantially higher than that of graphite, because graphene can adsorb lithium ions on both sides. Furthermore, the single layer of graphene provides a facile route for the diffusion of lithium ions, since the space for lithium intercalation is much larger than that in graphite interlayers.[29,31−33] Despite these advantages, graphene anodes experience significant irreversible capacity losses during charge/discharge cycling, mainly due to the restacking of graphene layers.[34] Recently, it was found that this problem can be alleviated by incorporating solid nanoparticles in between the sheets to reduce the restacking degree.[35−37]

In this work, we propose a novel approach to designing and synthesizing a graphene nanocomposite with Fe_2O_3 and SnO_2 particles, in which graphene, Fe_2O_3, and SnO_2 particles play different but complementary roles. Graphene serves as a matrix enabling both lithium ions and electrons to migrate to active sites, thereby fully maximizing the energy density. The graphene also is an effective elastic buffer to relieve the strain that would otherwise accumulate in the agglomerated Fe_2O_3 particles during Li uptake/release. In turn, the dispersion of Fe_2O_3 and SnO_2 particles on graphene prevents the restacking of graphene sheets, maintaining a high storage capacity of lithium during cycling. It is worth noting that the graphene used in this work is prepared via reduction of graphene oxide (GO) by $SnCl_2$, a nontoxic reducing agent, introducing SnO_2 in the same step. However, both the lithium insertion and extraction potentials of SnO_2 are below 0.7 V and just beyond the active potential range of Fe_2O_3 (0.7 to 2.0 V). Thus, due to the discrepancy in electrochemical active potentials, SnO_2 is expected to mainly serve as an inert matrix for Fe_2O_3 particles and keep them from agglomerating. This might be an important reason for the high performance observed from the graphene nanocomposite anode during the discharge−charge cycling.

EXPERIMENTAL SECTION

Materials Preparation. The rGO/Fe_2O_3/SnO_2 ternary nanocomposite was synthesized via an in situ precipitation of Fe_2O_3 nanoparticles using $FeCl_3$ precursor onto GO, followed by a subsequent reduction with $SnCl_2$ to obtain highly conductive reduced GO (rGO). Typically, GO aqueous solution was prepared through a modified Hummer's method by using natural graphite powder as a precursor.[38,39] In a typical synthesis procedure, $FeCl_3{\cdot}6H_2O$ (0.8 g) and urea (1.5 g) were added to 150 mL of GO solution (containing about 0.12 g GO) under constant stirring. After sonicating for 30 min, the suspension was transferred to a Teflon-lined autoclave and maintained at 120 °C for 4 h. Because the oxygen functional groups on the GO sheets can chemically bond with the metals ions, Fe^{3+} ions were likely anchored on the planes of the GO sheets.[40] Therefore, Fe^{3+} can be precipitated by OH^- on GO sheets when the urea decomposes during the hydrothermal process. In order to realize the reduction of GO, the suspension was adjusted to pH = 7.0 after cooling to room temperature. Then, $SnCl_2{\cdot}H_2O$ (0.23 g) was introduced into the above solution, and a temperature of 30 °C was maintained for 1.0 h with continuous magnetic stirring to achieve a maximum reduction efficiency. The resulting precipitation was washed with water and ethanol several times during the centrifuge separation process. Finally, the product was dried at 80 °C for 8 h, followed by an annealing treatment at 400 °C for 1.0 h under an Ar atmosphere to enhance the degree of crystallization of the Fe_2O_3 and SnO_2 in the ternary nanocomposite. For a comparison, traditional rGO was also prepared via a reduction of GO using hydrazine.

Physical Characterization. The prepared rGO/Fe_2O_3/SnO_2 ternary nanocomposites were studied using extensive characterization to determine their morphology and structure. The crystallinity of various samples was analyzed by X-ray diffraction (XRD) using a Bruker AXS D8 Advance diffractometer with Cu Kα radiation. The patterns were obtained at a scan rate of 5° min^{-1} with a step of 0.02°. X-ray photoelectron spectroscopy (XPS) was performed on an ESCA 210 and MICROLAB 310D spectrometer using an Mg Kα source. High-resolution spectra were acquired with 20 eV pass energy. The area of analysis was 700 × 300 μm in size, and each sample was analyzed at a 90° takeoff angle with a depth of 3−4 nm. Materials morphology was characterized by scanning electron microscopy (SEM) on an FEI Quanta 400 ESEM. High-resolution transmission electron microscopy (HR-TEM) images were taken on an FEI Titan 80-300 S/TEM. All Raman spectra were obtained using a Kaiser Holospec Raman system at 514 nm excitation focused through a 100× microscope objective for a total spot size of 1 μm. Excitation power was held constant at 150 μW for all samples. Four individual 30 s spectra were summed for a total integration time of 120 s. Fourier transform infrared (FTIR) spectra were also obtained using a BIO-RAD FTS 6000 system using the KBr pellet method. Thermogravimetric analysis (TGA) was performed on a Netzsch STA449C system.

Electrochemical and Battery Measurements. The anode electrode was prepared by mixing the rGO/Fe_2O_3/SnO_2 nanocomposite with acetylene black and polyvinylidene fluoride (PVDF) at a mass ratio of 80:10:10. The average coating thickness for the active materials is 16 μm with a diameter of 14 mm, when loading is 1.5 mg. A piece of Li metal foil was used as a combined counter and reference electrode. CR2025 type coin cell cases were assembled in a glovebox under Ar atmosphere, where both O_2 and H_2O levels were controlled below 5 ppm. The electrolyte was 1.0 M $LiPF_6$ in ethylene carbonate (EC) and dimethyl carbonate (DEC) with 1:1 volumetric ratio. The cyclic voltammograms (CV) were recorded on a CHI 750D electrochemical workstation from 0.02 to 3.0 V (vs. Li/Li^+) at a scan rate of 0.5 mVs^{-1}. Electrochemical impedance spectroscopy (EIS) was employed to measure the assembled coin cell on an Autolab electrochemical workstation. The frequency range is from 10^5 to 10^{-2} Hz with amplitude of 5 mV. The galvanostatic charge−discharge tests were carried out in a potential range from 0.04 to 3.0 V (vs. Li/Li^+) on an Arbin BT-2000 battery station.

RESULTS AND DISCUSSION

GO Reduction Using $SnCl_2$ as a Reducing Agent. Currently, the reduction mechanism of GO with Sn^{2+} remains unclear. Our investigation on the reduction of GO using $SnCl_2$ is discussed here. Upon the addition of Sn^{2+}, the carboxyl group on GO is able to chelate the Sn^{2+} ions, leading to formation of interlinked GO complexes as shown in Figure 1. As a result, the aggregation and precipitation of GO sheets occur. However, the interactions between Sn^{2+} and GO sheets are weak and can be broken by sonication.

As shown in Figure 2, we studied the GO reduction process as a function of solution temperature and reaction time by monitoring the solution color. With the removal of oxygen-containing functional groups on GO, the dark yellow GO

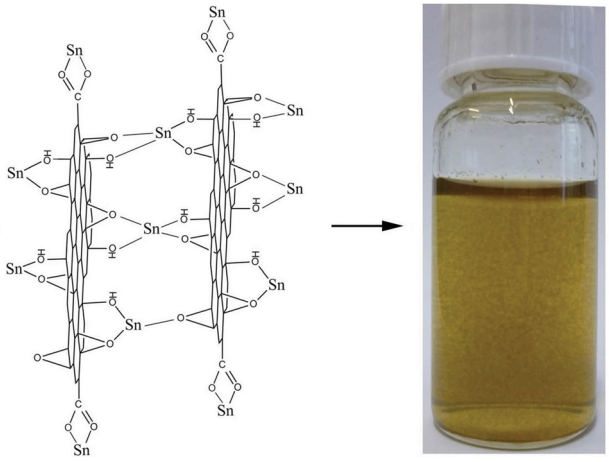

Figure 1. Schematic diagram for the interaction between Sn^{2+} and GO.

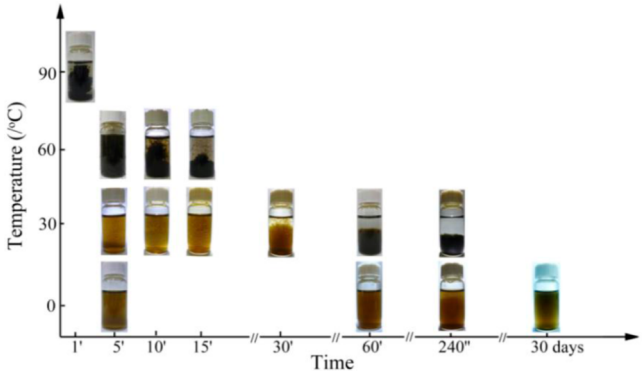

Figure 2. Reduction process of GO using $SnCl_2$ as functions of temperature and reduced time.

solution gradually changes to black, indicating a reduction of GO.[41] In the meantime, it was found that the reduction rate of GO is greatly dependent on the temperature when Sn^{2+} is used as a reducing agent. Below 0 °C, the reduction is sluggish and it takes more than one month. The precipitation formed can be easily recovered using sonication. At 30 °C, the irreversible formation of precipitation appears after 5 min and becomes significant at 30 min. A dark black solution was observed after 4 h, indicating a complete reduction process. Furthermore, at 60 °C, the precipitation appears after 5 min, followed by a complete reduction in 15 min. When temperature increases to 90 °C, GO reduction is completed in 1 min. Thus, the reduction rate can be improved by increasing the solution temperature.

However, it was found that higher reduction temperatures usually lead to incomplete reduction as demonstrated by XPS analysis (Table S1 and Figure S1, Supporting Information). Higher content of C(O)O was detected on reduced GO at 60 and 90 °C, relative to the GO reduced at 30 °C. In good agreement with the XPS analysis, Raman spectra of rGO prepared at different temperatures indicate that more defects and oxygen containing groups are present on rGO reduced at higher temperatures (Figure S2, Supporting Information).

Synthesis of rGO/Fe_2O_3/SnO_2 Nanocomposite. After optimizing the GO reduction process with $SnCl_2$ reducing agent, the synthesis of rGO/Fe_2O_3/SnO_2 ternary nanocomposite is carried out at 30 °C for 1.0 h as shown in Figure 3. It is believed that epoxy and alcohol groups are the dominant

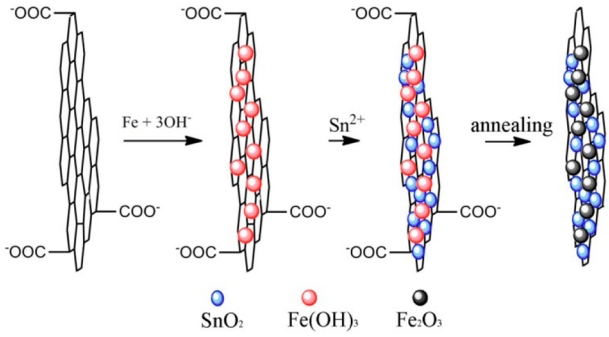

Figure 3. Scheme of preparation of ternary rGO/Fe_2O_3/SnO_2 nanocomposite.

oxygen-containing functionalities on the plane of GO, which can be easily reduced. However, a complete reduction of GO flakes requires use of a very strong reducing agent and high temperature thermal annealing, which also introduces a number of defects.[42] In this work, using the relatively weak reducing agent $SnCl_2$, the reduction of GO is mainly aimed to eliminate the epoxy and hydroxyl groups from the basal planes.

Structure and Morphology. Further insights into the structural changes in the carbon lattice of rGO after incorporating oxide particles were explored using Raman spectroscopy (Figure 4). These spectra are dominated by

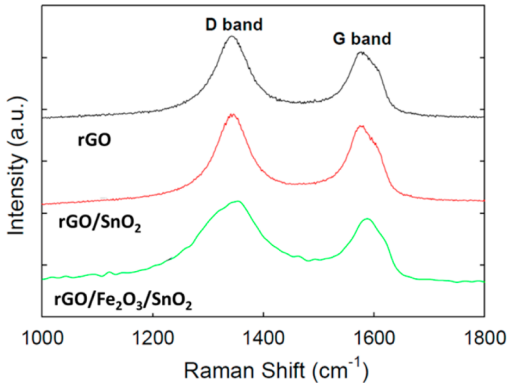

Figure 4. Raman spectra for rGO, rGO/SnO_2, and rGO/Fe_2O_3/SnO_2.

characteristic carbon resonances around 1600 cm^{-1} (G band) and 1350 cm^{-1} (D band), which correspond to the planar motion of sp^2-hybridized carbon atoms in an ideal graphene layer and to the carbon atoms close to the edge of graphene sheets, respectively. The D-band/G-band ratios (I_D/I_G) of these peaks provide an indication of the degree of ordering of the rGO flakes. The calculated ratios for rGO and rGO/SnO_2 are 1.2 and 1.1, respectively. This indicates a higher disorder of rGO reduced by hydrazine, relative to rGO reduced by $SnCl_2$. This disorder is likely due to the doping of nitrogen atoms into graphene planes, when hydrazine was used as a reducing agent.[43] Compared to rGO/SnO_2, the I_D/I_G of the ternary rGO/Fe_2O_3/SnO_2 is 1.3, suggesting a lower proportion of carbon atoms with hexagonal symmetry, i.e., in the interior of graphene sheets. The larger full-width-at-half-maximum (fwhm) of the D band observed with the rGO/Fe_2O_3/SnO_2 also indicates a higher degree of disorder relative to the other two samples.

The XRD pattern for rGO/Fe_2O_3/SnO_2 shown in Figure 5a indicates that the main peaks observed with the nanocomposite

dx.doi.org/10.1021/am402124r | ACS Appl. Mater. Interfaces 2013, 5, 8607−8614

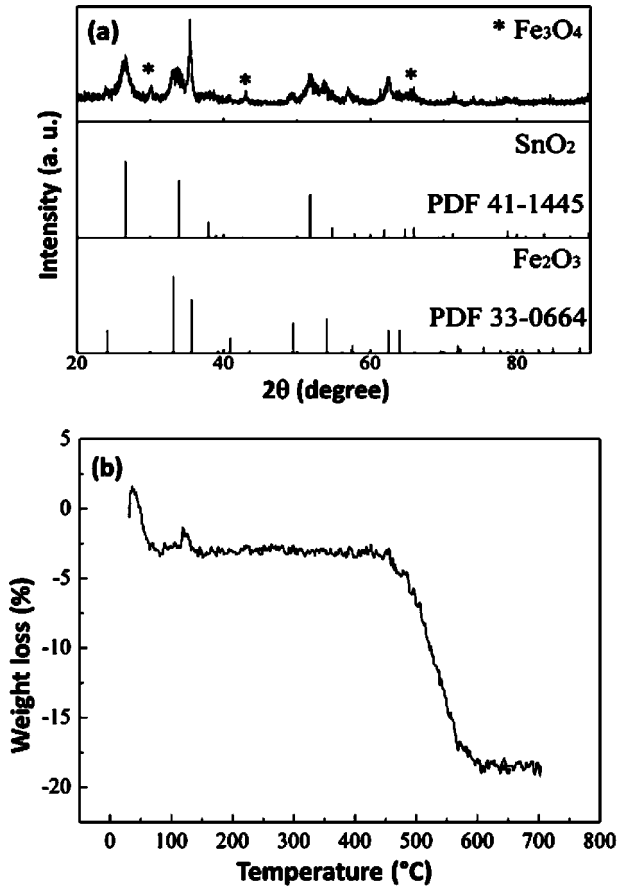

Figure 5. (a) XRD pattern and (b) TGA curve for the rGO/Fe_2O_3/SnO_2 nanocomposite.

match well with those of standard rhombohedral Fe_2O_3 (JCPDF: 33−0664) and tetragonal rutile SnO_2 (JCPDF: 41−1445). In addition, the diffraction peaks marked with asterisks can be ascribable to Fe_3O_4, indicating that some Fe^{3+} ions were reduced to Fe^{2+} during the GO reduction using $SnCl_2$ as a reducing agent. As Fe_3O_4 is also an active component in LIB anodes capable of accommodating Li^+,[44,45] it is not considered as an "impurity" here. The weight percentages of rGO in the rGO/Fe_2O_3/SnO_2 ternary composite was determined to be 18 wt % by calculating the TGA curve as shown in Figure 5b.

The C 1s XPS spectrum of rGO/Fe_2O_3/SnO_2 composite (Figure 6a) presents a dominant C−C peak in graphene planes, accompanied by two minor peaks corresponding to C−OH and C(O)O groups,[10] respectively. The results are indicative of a successful reduction of GO when $SnCl_2$ is used as the reducing agent. The Sn 3d binding energies at 486.9 and 495.4 eV shown in Figure 6b are ascribed to Sn(II). In Figure 6c, the peaks at 712.2 and 725.6 eV are attributed to Fe 2p3/2 and Fe 2p1/2, respectively, attesting to the presence of Fe(III). The shoulder peak at around 710 eV provides further evidence of Fe_3O_4, in good agreement with XRD analysis indicating a partial reduction of Fe^{3+} into Fe^{2+} by $SnCl_2$. The FTIR spectrum of the ternary composite is shown in Figure 6d. The strongest peak at 626 cm^{-1} is assigned to Sn−O, and two sharp bands at 576 and 478 cm^{-1} can be attributed to the stretching vibrations of the Fe^{3+}−O^{2-} bond in the FeO_6 octahedron and FeO_4 tetrahedron structures,[46] respectively. In addition, three weak bands at 1712, 1575, and 1207 cm^{-1} correspond to COOH, C−C, and C−OH stretching. Thus, the FTIR results clearly verify the formation of SnO_2 and Fe_2O_3 incorporated into the rGO during the synthesis.

The morphology of the rGO/Fe_2O_3/SnO_2 nanocomposite was characterized using SEM images (Figure S3, Supporting Information). It can be seen that metal oxides particles are adsorbed on both sides of the graphene sheet and the obtained graphene has multiple layers. The contents of SnO_2, Fe_2O_3, and C are calculated to be 54.7, 29.9, and 15.4 wt % from EDS, respectively. The total content of metal oxides is in good agreement with the TGA result. The particles in Figure S3, Supporting Information, exhibit an irregular shape, with particle size ranging from 20 to 50 nm.

TEM images in Figure 7a,b also indicate that the metal oxide particles are well dispersed on the graphene flakes with an average size of about 20 nm. Such fine particle morphology can

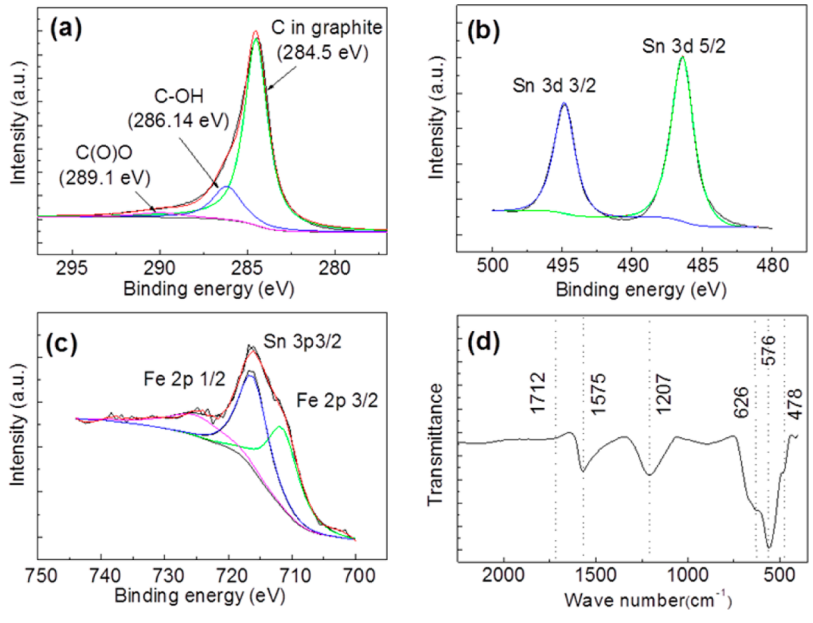

Figure 6. XPS spectra of (a) C 1s, (b) Sn 3d, (c) Fe 2p, and (d) FTIR spectrum of rGO/Fe_2O_3/SnO_2 nanocomposites.

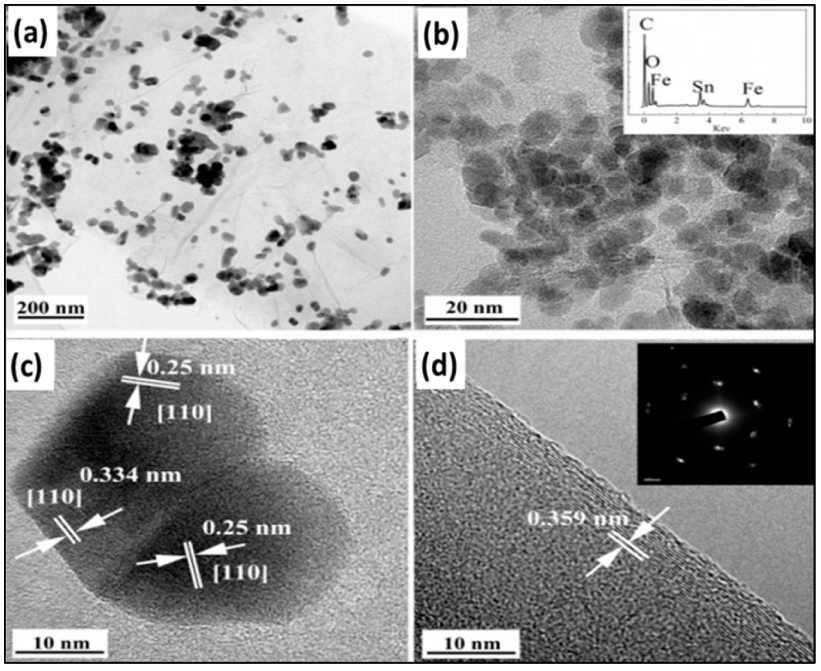

Figure 7. Morphology and structure of the rGO/Fe_2O_3/SnO_2/ nanocomposites: (a, b) TEM images under different magnifications (the inset is the EDS spectra), (c) Fe_2O_3 and SnO_2 nanoparticles on rGO, and (d) HR-TEM image of rGO planes (the inset is the SAED pattern of rGO).

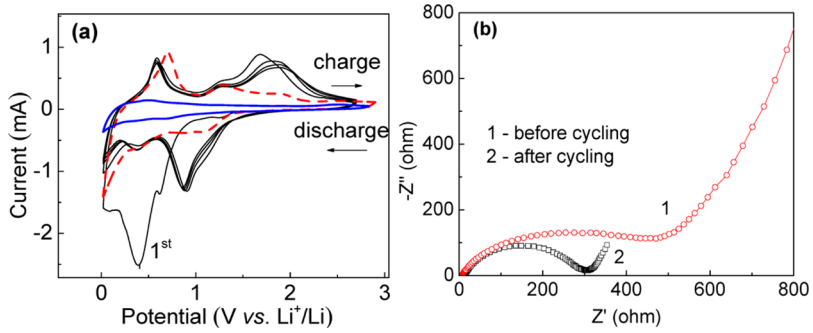

Figure 8. (a) CV curves up to four cycles for the rGO/Fe_2O_3/SnO_2/ nanocomposites as well as the CV profiles for individual SnO_2 (red dashed line) and rGO (blue solid line); (b) the Nyquist plots for EIS of the rGO/Fe_2O_3/SnO_2/ nanocomposites after and before cycling.

shorten the diffusion pathway of Li^+ ions and accelerate electron transport, thus greatly improving the lithium storage ability and rate performance of the anode. Two lattice interlayer distances of 0.250 and 0.343 nm are also observed in the HR-TEM images (Figure 7c) and could most likely be assigned to the (110) crystal planes of Fe_2O_3 crystals (JCPDS 33−0664) and the (110) planes of SnO_2 (JCPDS 41−1445), respectively. Importantly, well separated Fe_2O_3 and SnO_2 nanoparticles are demonstrated in Figure 7c, suggesting a promotional role of SnO_2 capable of preventing Fe_2O_3 particle aggregation. Figure 7d exhibits the TEM image of rGO having a multilayered structure. The measured lattice interlayer distance of 0.359 nm is larger than that of standard graphite (0.335 nm), due to an expansion effect induced by the remaining oxygen-containing species on the rGO. The inserted selected area electron diffraction (SAED) image of graphene in Figure 7d shows a typical hexagonal pattern of graphene, further indicating that the reduction of GO using $SnCl_2$ in this work results in an effective restoration of the π-conjugated structure, thereby yielding highly electronic conductive graphene materials.[42]

Electrochemical Properties. The CV curves shown in Figure 8a clearly illustrate the different lithium insertion/extraction potentials of Fe_2O_3, SnO_2, and rGO. In the first discharge process of rGO/Fe_2O_3/SnO_2/ nanocomposite, a couple of minor cathodic peaks observed at potentials of 1.2 and 0.7 V are related to the possible reduction from Fe_2O_3 to Fe as shown below[47]

$$Fe_2O_3 + 2Li^+ + 2e^- \rightarrow Li_2(Fe_2O_3) \quad (3)$$

$$Li_2(Fe_2O_3) + 4Li^+ + 4e^- \rightarrow Fe^0 + 3Li_2O \quad (4)$$

$$2Fe^0 + 2Li_2O \leftrightarrow 2Fe^{II}O + 4Li^+ + 4e^- \quad (5)$$

The large irreversible cathodic peak appearing at 0.3 V is associated with the formation of solid electrolyte interphase (SEI).[48] In addition, reduction of SnO_2 to metallic Sn is also likely according to[49]

$$SnO_2 + 4Li^+ + 4e^- \rightarrow Sn + 2Li_2O \quad (6)$$

The peak close to 0.0 V is related to the insertion of Li into metallic Sn and graphene. In the subsequent cycles, a pair of peaks observed at potentials of 0.02/0.59 V (cathodic/anodic) can be assigned to the reversible alloying/dealloying processes of Li_xSn ($0 \leq x \leq 4.4$). Another pair of peaks located at

dx.doi.org/10.1021/am402124r | ACS Appl. Mater. Interfaces 2013, 5, 8607−8614

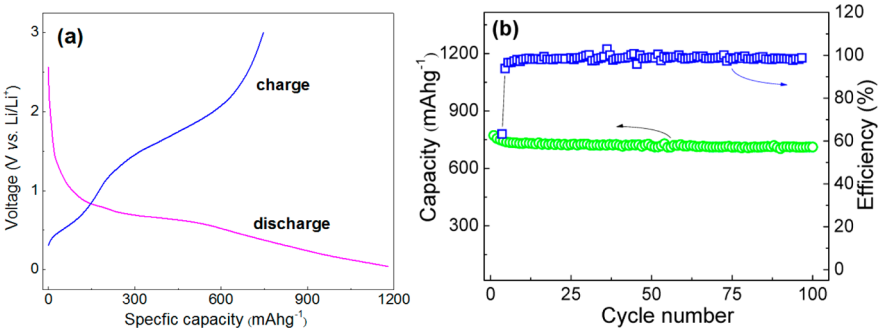

Figure 9. Lithium storage properties of the rGO/Fe_2O_3/SnO_2 nanocomposites: (a) initial discharge–charge voltage profiles; (b) discharge capacity and efficiency as a function of cycle numbers at a current density of 400 mAg^{-1}.

potentials of 0.87/1.86 V (cathodic/anodic) results from the reversible displacive redox reactions of Fe_2O_3.[4,10] In the meantime, the CV profile of individual SnO_2 as shown in Figure 8a only exhibits one couple of notable reversible peaks at potentials of 0.02/0.59 V, corresponding to alloying and dealloying of Li_xSn. In addition, a pair of weak peaks at 1.0/1.2 V is thought to be related to the reversible decomposition of Li_2O. No obvious peak can be observed in the CV profile of the pure rGO electrode. Thus, lithiation and delithiation of Fe_2O_3 nanoparticles occur at higher potentials than those of SnO_2 and rGO. Thus, the SnO_2 and rGO components in the ternary composite may serve as inert matrices to prevent Fe_2O_3 nanoparticles from aggregation during discharge–charge cycling. As a result, the unique composite structure can sustain a large specific surface area of Fe_2O_3 for Li intercalation and extraction.

As shown in the Nyquist plots (Figure 8b), the charge transfer resistance (R_p) of the rGO/Fe_2O_3/SnO_2 composite anode was found to be significantly reduced after the first cycle, mainly due to the reduction of SnO_2 to metallic Sn. As the lithium insertion and extraction reaction rates in the anode are governed by Li diffusivity and electron conductivity, the improved electronic conductivity resulting from formation of metallic Sn during the first cycle would be beneficial for reducing the charge transfer resistance. It is also likely that the volume expansion of SnO_2 and Fe_2O_3 particles during the first discharge will help increase the interspace between rGO sheets, providing larger spaces for Li diffusion and thus facilitating charge transfer.

Lithium Ion Battery Tests. Battery tests show that the prepared rGO/Fe_2O_3/SnO_2 ternary composite anode exhibits a good activity for Li insertion/extraction and cycling stability. In particular, at a charge/discharge current density of 400 mAg^{-1} (Figure 9a), the first discharge (Li insertion) and charge (Li extraction) capacities were 1179 and 746 $mAhg^{-1}$, respectively. During the subsequent 100 cycles (Figure 9b), the discharge capacity was maintained above 700 $mAhg^{-1}$. During the cyclic testing, an average columbic efficiency of 98% was achieved (right *Y* axis in Figure 9b) except for a few cycles at the initial stage, indicating a good capacity retention during the discharge–charge tests.

The rate performance of the ternary rGO/Fe_2O_3/SnO_2 graphene anode was studied at each discharge–charge rate for 10 cycles, as shown in Figure 10. The theoretical capacities for SnO_2 and Fe_2O_3 are 780 and 1000 $mAhg^{-1}$, respectively. As Li ions are able to adsorb on both sides of a graphene sheet (Li_2C_6),[1,50] the capacity calculated for rGO is about 744

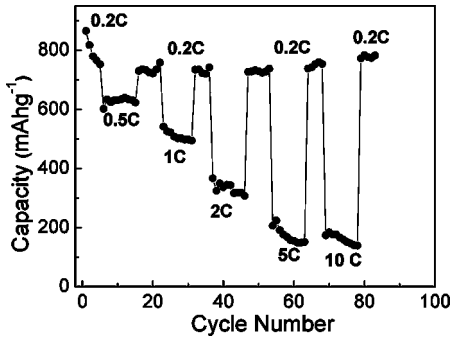

Figure 10. Rate performance of the rGO/Fe_2O_3/SnO_2 composite anode determined at different current densities.

$mAhg^{-1}$. Thus, the theoretical specific capacity of 841 $mAhg^{-1}$ for the ternary composite was determined by

$$C_{rGO/Sn/Fe/} = C_{rGO} \times 15.4\% + C_{Fe} \times 29.9\% + C_{Sn} \times 54.7\% \quad (7)$$

where $C_{rGO/Sn/Fe/}$, C_{rGO}, C_{Fe}, and C_{Sn} correspond to the theoretical capacities of rGO/Fe_2O_3/SnO_2, rGO, Fe_2O_3, and SnO_2, respectively. The mass percentages for individual components were determined by EDS. During the rate performance tests, the charge–discharge cycles were started with a low current rate of 0.2*C* (1 *C* = 841 mAg^{-1}) in the first 5 cycles, and then, the rates were gradually increased up to 10*C*. The reversible capacities were measured to be 623 $mAhg^{-1}$ at 0.5*C*, 493 $mAhg^{-1}$ at 1*C*, 307 $mAhg^{-1}$ at 2*C*, 154 $mAhg^{-1}$ at 5*C*, and 139 $mAhg^{-1}$ at 10*C*. The decreased capacity at a higher current rate can be explained by an increasing resistance at the interface between the electrolyte and the active materials as well as insufficient Li diffusivity at high rates.[51,52] It is worth noting that a reversible capacity of 782 $mAhg^{-1}$ was recovered after decreasing the charge rate from 10*C* to 0.2*C*, indicating an excellent capacity reversibility and cycle stability.

As shown in Figure 11, the ternary anode material studied in this work is superior to rGO and binary rGO/SnO_2 materials, showing improved cycle stability and specific capacity. The rGO anode exhibits a reversible capacity of 550 $mAhg^{-1}$ at a current density of 400 mAg^{-1} after 100 cycles, indicating a capacity loss of 18%. Although the resistance of the rGO/Fe_2O_3/SnO_2 nanocomposite revealed in the EIS (Figure S4, Supporting Information) is higher than that of SnO_2/rGO due to the low electronic conductivity of Fe_2O_3, the charge capacities measured with the rGO/Fe_2O_3/SnO_2 composite during 100 cycles is significantly larger, relative to those of

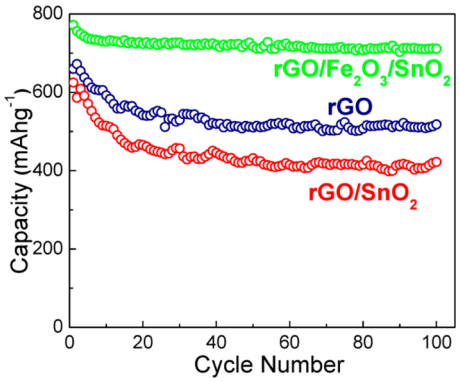

Figure 11. Comparison of discharge−charge capacity measured with rGO, rGO/SnO_2, and rGO/Fe_2O_3/SnO_2 anodes up to 100 cycles.

rGO/SnO_2. In particular, in the absence of Fe_2O_3, the rGO/SnO_2 anode shows worse performance with a capacity of 600 mAhg^{-1} at the first discharge−charge cycle, followed by approximately 30% capacity loss after 100 cycles. While initial performance loss was also observed with the ternary graphene composite anode, a specific capacity of above 700 mAhg^{-1} can be retained during the subsequent 100 cycles, demonstrating much improved cyclic stability.

The enhanced cycle stability and capacity observed with the rGO/Fe_2O_3/SnO_2 anode can be attributed to the complementary roles among Fe_2O_3, SnO_2, and rGO structures. In addition, a higher degree of disorder in the rGO/Fe_2O_3/SnO_2 composite, as demonstrated by Raman analysis (Figure S4, Supporting Information), may facilitate the Li adsorption/desorption on graphene planes.[33] Thus, on the basis of all of these advantages observed in the ternary composite, the lithium storage ability and cycle stability of rGO/Fe_2O_3/SnO_2 nanocomposite anode are significantly improved relative to rGO and rGO/SnO_2 materials.

CONCLUSIONS

In this work, we developed an rGO/Fe_2O_3/SnO_2 ternary nanocomposite via an in situ precipitation of Fe_2O_3 nanoparticles on GO, followed by a subsequent chemical reduction of GO with $SnCl_2$. The ternary anode exhibits a highly stable capacity during discharge−charge cyclic testing in lithium ion batteries. The graphene component provides for a conductive matrix facilitating transfer of lithium ions and electrons and also serves as an effective elastic buffer to relieve the stress that would otherwise accumulate in the Fe_2O_3 particles during Li uptake/release. The dispersion of Fe_2O_3 and SnO_2 particles on graphene mitigates the degree of stacking of graphene sheets. In addition, SnO_2 particles hinder the agglomeration of Fe_2O_3 nanoparticles. As a result, the novel nanocomposite exhibits initial discharge and charge capacities of 1179 and 746 mAhg^{-1}, respectively, at a current density of 400 mAg^{-1}. Furthermore, the discharge and charge capacities during 100 cycles were maintained above 700 mAhg^{-1}. The results of this study indicate that the rGO/Fe_2O_3/SnO_2 ternary nanocomposite holds great promise as a high performance anode material in Li ion batteries.

ASSOCIATED CONTENT

Supporting Information

Less-essential XPS, SEM, Raman, and EIS characterization. This information is available free of charge via the Internet at http://pubs.acs.org/.

AUTHOR INFORMATION

Corresponding Authors

*E-mail: wugang@lanl.gov. Phone: 505-665-0659.
*E-mail: lininghit@263.net. Phone: +86-451-83613721.

Notes

The authors declare no competing financial interest.

ACKNOWLEDGMENTS

Financial support from the Los Alamos National Laboratory Early Career Laboratory-Directed Research and Development (LDRD) Program (20110483ER) for this work is gratefully acknowledged.

REFERENCES

(1) Dahn, J. R.; Zheng, T.; Liu, Y.; Xue, J. S. *Science* **1995**, *270*, 590−593.
(2) Chan, C. K.; Peng, H.; Liu, G.; McIlwrath, K.; Zhang, X. F.; Huggins, R. A.; Cui, Y. *Nat. Nanotechnol.* **2008**, *3*, 31−35.
(3) Armand, M.; Tarascon, J. M. *Nature* **2008**, *451*, 652−657.
(4) Chen, Z.; Dai, C.; Wu, G.; Nelson, M.; Hu, X.; Zhang, R.; Liu, J.; Xia, J. *Electrochim. Acta* **2010**, *55*, 8595−8599.
(5) Xu, X.; Cao, R.; Jeong, S.; Cho, J. *Nano Lett.* **2012**, *12*, 4988−4991.
(6) Han, F.-D.; Bai, Y.-J.; Liu, R.; Yao, B.; Qi, Y.-X.; Lun, N.; Zhang, J.-X. *Adv. Energy Mater.* **2011**, *1*, 798−801.
(7) Chan, C. K.; Patel, R. N.; O'Connell, M. J.; Korgel, B. A.; Cui, Y. *ACS Nano* **2010**, *4*, 1443−1450.
(8) Zhu, X.; Zhu, Y.; Murali, S.; Stoller, M. D.; Ruoff, R. S. *ACS Nano* **2011**, *5*, 3333−3338.
(9) Liu, R.; Li, N.; Xia, G.; Li, D.; Wang, C.; Xiao, N.; Tian, D.; Wu, G. *Mater. Lett.* **2013**, *93*, 243−246.
(10) Zhu, J. X.; Lu, Z. Y.; Oo, M. O.; Hng, H. H.; Ma, J.; Zhang, H.; Yan, Q. Y. *J. Mater. Chem.* **2011**, *21*, 12770−12776.
(11) Li, W. Y.; Xu, L. N.; Chen, J. *Adv. Funct. Mater.* **2005**, *15*, 851−857.
(12) Han, Y.; Wang, Y.; Li, L.; Wang, Y.; Jiao, L.; Yuan, H.; Liu, S. *Electrochim. Acta* **2011**, *56*, 3175−3181.
(13) Song, Y.; Qin, S.; Zhang, Y.; Gao, W.; Liu, J. *J. Phys. Chem. C* **2010**, *114*, 21158−21164.
(14) Reddy, M. V.; Yu, T.; Sow, C. H.; Shen, Z. X.; Lim, C. T.; Subba Rao, G. V.; Chowdari, B. V. R. *Adv. Funct. Mater.* **2007**, *17*, 2792−2799.
(15) Jia, X.; Chen, J.-J.; Xu, J.-H.; Shi, Y.-N.; Fan, Y.-Z.; Zheng, M.-S.; Dong, Q.-F. *Chem. Commun.* **2012**, *48*, 7410−7412.
(16) Lin, Y.-M.; Abel, P. R.; Heller, A.; Mullins, C. B. *J. Phys. Chem. Lett.* **2011**, *2*, 2885−2891.
(17) Deng, D.; Lee, J. Y. *Chem. Mater.* **2008**, *20*, 1841−1846.
(18) Jiang, Y.; Yuan, T.; Sun, W.; Yan, M. *ACS Appl. Mater. Interfaces* **2012**, *4*, 6216−6220.
(19) Zhong, C.; Wang, J.; Chen, Z.; Liu, H. *J. Phys. Chem. C* **2011**, *115*, 25115−25120.
(20) Wang, L.; Wang, D.; Dong, Z.; Zhang, F.; Jin, J. *Nano Lett.* **2013**, *13*, 1711−1716.
(21) Lin, J.; Peng, Z.; Xiang, C.; Ruan, G.; Yan, Z.; Natelson, D.; Tour, J. M. *ACS Nano* **2013**, *7*, 6001−6006.
(22) Tarascon, J. M.; Armand, M. *Nature* **2001**, *414*, 359−367.
(23) Hertzberg, B.; Alexeev, A.; Yushin, G. *J. Am. Chem. Soc.* **2010**, *132*, 8548−8549.
(24) Poizot, P.; Laruelle, S.; Grugeon, S.; Dupont, L.; Tarascon, J. M. *Nature* **2000**, *407*, 496−499.

(25) Arico, A. S.; Bruce, P.; Scrosati, B.; Tarascon, J.-M.; van Schalkwijk, W. *Nat. Mater.* **2005**, *4*, 366−377.
(26) Chen, J.; Xu, L.; Li, W.; Gou, X. *Adv. Mater.* **2005**, *17*, 582−586.
(27) Stankovich, S.; Dikin, D. A.; Dommett, G. H. B.; Kohlhaas, K. M.; Zimney, E. J.; Stach, E. A.; Piner, R. D.; Nguyen, S. T.; Ruoff, R. S. *Nature* **2006**, *442*, 282−286.
(28) Yoo, E.; Kim, J.; Hosono, E.; Zhou, H.-s.; Kudo, T.; Honma, I. *Nano Lett.* **2008**, *8*, 2277−2282.
(29) Wang, C.; Li, D.; Too, C. O.; Wallace, G. G. *Chem. Mater.* **2009**, *21*, 2604−2606.
(30) Wu, G.; Mack, N. H.; Gao, W.; Ma, S.; Zhong, R.; Han, J.; Baldwin, J. K.; Zelenay, P. *ACS Nano* **2012**, *6*, 9764−9776.
(31) Lian, P.; Zhu, X.; Liang, S.; Li, Z.; Yang, W.; Wang, H. *Electrochim. Acta* **2010**, *55*, 3909−3914.
(32) Wang, G.; Shen, X.; Yao, J.; Park, J. *Carbon* **2009**, *47*, 2049−2053.
(33) Wu, Z.-S.; Ren, W.; Xu, L.; Li, F.; Cheng, H.-M. *ACS Nano* **2011**, *5*, 5463−5471.
(34) Evanoff, K.; Magasinski, A.; Yang, J.; Yushin, G. *Adv. Energy Mater.* **2011**, *1*, 495−498.
(35) Yang, S.; Feng, X.; Ivanovici, S.; Müllen, K. *Angew. Chem., Int. Ed.* **2010**, *49*, 8408−8411.
(36) Wang, H.; Cui, L.-F.; Yang, Y.; Sanchez Casalongue, H.; Robinson, J. T.; Liang, Y.; Cui, Y.; Dai, H. *J. Am. Chem. Soc.* **2010**, *132*, 13978−13980.
(37) Zhou, G.; Wang, D.-W.; Li, F.; Zhang, L.; Li, N.; Wu, Z.-S.; Wen, L.; Lu, G. Q.; Cheng, H.-M. *Chem. Mater.* **2010**, *22*, 5306−5313.
(38) Hummers, W. S.; Offeman, R. E. *J. Am. Chem. Soc.* **1958**, *80*, 1339−1339.
(39) Marcano, D. C.; Kosynkin, D. V.; Berlin, J. M.; Sinitskii, A.; Sun, Z.; Slesarev, A.; Alemany, L. B.; Lu, W.; Tour, J. M. *ACS Nano* **2010**, *4*, 4806−4814.
(40) Ramesha, G. K.; Sampath, S. *J. Phys. Chem. C* **2009**, *113*, 7985−7989.
(41) McAllister, M. J.; Li, J.-L.; Adamson, D. H.; Schniepp, H. C.; Abdala, A. A.; Liu, J.; Herrera-Alonso, M.; Milius, D. L.; Car, R.; Prud'homme, R. K.; Aksay, I. A. *Chem. Mater.* **2007**, *19*, 4396−4404.
(42) Pei, S.; Zhao, J.; Du, J.; Ren, W.; Cheng, H.-M. *Carbon* **2010**, *48*, 4466−4474.
(43) He, Q.; Li, Q.; Khene, S.; Ren, X.; López-Suárez, F. E.; Lozano-Castelló, D.; Bueno-López, A.; Wu, G. *J. Phys. Chem. C* **2013**, *117*, 8697−8707.
(44) Kang, E.; Jung, Y. S.; Cavanagh, A. S.; Kim, G.-H.; George, S. M.; Dillon, A. C.; Kim, J. K.; Lee, J. *Adv. Funct. Mater.* **2011**, *21*, 2430−2438.
(45) Muraliganth, T.; Vadivel Murugan, A.; Manthiram, A. *Chem. Commun.* **2009**, *0*, 7360−7362.
(46) Moustafa, Y. M.; El-Egili, K.; Doweidar, H.; Abbas, I. *Phys. B: Condens. Matter* **2004**, *353*, 82−91.
(47) Chowdari, B. V. R.; Reddy, M. V.; Yu, T.; Sow, C. H.; Shen, Z. X.; Lim, C. T.; Rao, G. V. S. *Adv. Funct. Mater.* **2007**, *17*, 2792−2799.
(48) Peled, E. *J. Electrochem. Soc.* **1979**, *126*, 2047−2051.
(49) Courtney, I. A.; Dahn, J. R. *J. Electrochem. Soc.* **1997**, *144*, 2045−2052.
(50) Zhang, M.; Lei, D.; Yin, X.; Chen, L.; Li, Q.; Wang, Y.; Wang, T. *J. Mater. Chem.* **2010**, *20*, 5538−5543.
(51) Han, J.; Zhu, J.; Li, Y.; Yu, X.; Wang, S.; Wu, G.; Xie, H.; Vogel, S. C.; Izumi, F.; Momma, K.; et al. *Chem. Commun.* **2012**, *48*, 9840−9842.
(52) Kim, H.; Wen, Z.; Yu, K.; Mao, O.; Chen, J. *J. Mater. Chem.* **2012**, *22*, 15514−15518.